21 September 2026

Fracture mechanics favors lower-than-expected stack pressures in halide solidstate batteries

Liqun Guo[1], Jie Zheng[1], Lihong Zhao[1], Santosh Thapa[2], Yanliang Liang[1], Phat Tieu[1], Mai Le[1], Yang-Tse Cheng[2], Robert L. Sacci[3], Jagjit Nanda[4,5], Yan Yao[1,6,7]

1. Department of Electrical and Computer Engineering and Texas Center for Superconductivity, University of Houston
2. Department of Physics and Astronomy, University of Kentucky
3. Chemical Sciences Division, Oak Ridge National Laboratory
4. Applied Energy Division, SLAC National Laboratory
5. Department of Materials Science and Engineering, Stanford University
6. Department of Earth and Environmental Engineering, Columbia University
7. Columbia Climate School, Columbia University

Abstract

All-solid-state batteries promise safer, more energy-dense storage than cells built on liquid electrolytes. Among solid-state electrolytes, halide electrolytes offer high ionic conductivity, anodic stability, and room-temperature processability, yet stable cycling is typically achieved under stack pressures of tens to hundreds of megapascals, for reasons that remain unclear. Here we identify the unusually high susceptibility of brittle halide electrolytes to fracture as the mechanism underlying and show that stack pressure—conventionally applied to suppress mechanical damage—can instead promote it by enhancing strain transfer from the active materials to the surrounding electrolyte. Operando scanning electron microscopy captures crack initiation and propagation within electrolyte domains in composite cathodes driven by active material volume changes, while nanoindentation reveals an exceptionally low fracture toughness of 0.23 MPa·m1/2 for the representative halide electrolyte Li3YCl6, substantially lower than the 0.7−1.0 MPa·m1/2 for typical sulfide and oxide electrolytes. Pressure-dependent electrochemical and morphological analyses show that, although modest pressure is sufficient to maintain interparticle contact, increasing pressure beyond this level promotes electrolyte fracture and accelerates capacity loss. Guided by this insight, we demonstrate an anode-free halide pouch cell that retains 85% of its capacity over 200 cycles at C/3 under only 2 MPa. Together, these findings show that the high stack pressures widely used in halide solid-state batteries primarily compensate for the consequences of electrolyte

Posted on 21 September 2026 — CC-BY 4.0 — This is a preprint and has not been peer reviewed. Data may be preliminary. — https://doi.org/10.26434/chemrxiv.15009212/v1

fracture rather than reflecting the pressure intrinsically required for stable operation, establishing a mechanical basis for low-pressure halide solid-state batteries.

Posted on 21 September 2026 — CC-BY 4.0 — This is a preprint and has not been peer reviewed. Data may be preliminary. — https://doi.org/10.26434/chemrxiv.15009212/v1

Fracture mechanics favors lower-than-expected stack pressures in halide solid-state batteries

Liqun Guo[1]†, Jie Zheng[1]†, Lihong Zhao[1]†, Santosh Thapa[2], Yanliang Liang[1], Phat Tieu[1], Mai Le[1], Yang-Tse Cheng[2], Robert L. Sacci[3], Jagjit Nanda[4,5]*, Yan Yao[1,6,7]**

Affiliations:

[1]Department of Electrical and Computer Engineering and Texas Center for Superconductivity at the University of Houston, University of Houston, Houston, TX 77204, USA.

[2]Department of Physics and Astronomy, University of Kentucky, Lexington, KY 40506, USA.

[3]Chemical Sciences Division, Oak Ridge National Laboratory, Oak Ridge, TN 37831, USA.

[4]Applied Energy Division, SLAC National Laboratory, Menlo Park, CA 94025, USA.

[5]Department of Materials Science and Engineering, Stanford University, Stanford, CA 94305, USA

[6]Department of Earth and Environmental Engineering, Columbia University; New York, NY 10027, USA

[7]Columbia Climate School, Columbia University; New York, NY 10027, USA

† These authors contributed equally to this work. *Corresponding author. saccirl@ornl.gov (R.L.S); jnanda@slac.stanford.edu (J.N.); yy3784@columbia.edu (Y.Y.)

Abstract

All-solid-state batteries promise safer, more energy-dense storage than cells built on liquid electrolytes[1, 2]. Among solid-state electrolytes, halide electrolytes offer high ionic conductivity, anodic stability, and room-temperature processability[3, 4], yet stable cycling is typically achieved under stack pressures of tens to hundreds of megapascals, for reasons that remain unclear. Here we identify the unusually high susceptibility of brittle halide electrolytes to fracture as the mechanism underlying and show that stack pressure—conventionally applied to suppress mechanical damage—can instead promote it by enhancing strain transfer from the active materials to the surrounding electrolyte. Operando scanning electron microscopy captures crack initiation and propagation within electrolyte domains in composite cathodes driven by active material volume changes, while nanoindentation reveals an exceptionally low fracture toughness of 0.23 $MPa \cdot m^{1/2}$ for the representative halide electrolyte Li_3YCl_6, substantially lower than the 0.7−1.0 $MPa \cdot m^{1/2}$ for typical sulfide and oxide electrolytes. Pressure-dependent electrochemical and morphological analyses show that, although modest pressure is sufficient to maintain interparticle contact, increasing pressure beyond this level promotes electrolyte fracture and accelerates capacity loss. Guided by this insight, we demonstrate an anode-free halide pouch cell that retains 85% of its capacity over 200 cycles at C/3 under only 2 MPa. Together, these findings show that the high stack pressures widely used in halide solid-state batteries primarily compensate for the consequences of electrolyte fracture rather than reflecting the pressure intrinsically required for stable operation, establishing a mechanical basis for low-pressure halide solid-state batteries.

All-solid-state batteries (ASSBs) are widely regarded as a promising technology for safer, higher-energy electric vehicles[1, 2]. Among solid-state electrolytes (SSEs), halides have emerged as leading candidates owing to their unique combination of room-temperature compressibility and high-voltage stability, enabling practical high-energy cell designs[3, 4]. However, halide ASSBs have yet to overcome a curious obstacle: stable operation is typically achieved under unusually high stack pressures. A survey of 58 recent studies shows that 67% employ pressures above 50 MPa and only 10% operate below 10 MPa (Supplementary Fig. 1, Supplementary Table 1). The practical consequences are substantial, including heavier cell packaging, incompatibility with lithium metal anodes, and diminished system-level energy density.

The origin of this high stack-pressure requirement remains elusive. It is frequently attributed to broadly defined mechanical degradation, such as loss of interparticle contact during cycling, yet this explanation is difficult to reconcile with sulfide-based ASSBs which rely on the same solid-solid contacts but routinely operate below 10 MPa[5-7]. Recent work by Yun *et al.* further demonstrated that the mechanical degradation of halide composite cathodes is primarily driven by cracking-induced deformation of halide electrolytes[8]. This important advance nevertheless still does not explain why halide electrolytes crack so readily under conditions that sulfides can tolerate.

This lack of mechanistic understanding has driven efforts for reducing stack pressure to engineer away from a fully-halide architecture, including the development of mechanically compliant oxyhalide electrolytes[9, 10] and the incorporation of compliant phases into composite cathodes[11]. These strategies effectively reduce the required pressure while often compromising electrochemical stability, ionic conductivity, or material simplicity. These efforts highlight the need for a mechanistic framework that explains why high stack pressures have appeared indispensable for halide ASSBs.

Here we identify fracture of brittle halide electrolytes as the governing degradation mechanism underlying the high stack-pressure requirement in halide ASSBs. Operando SEM and mechanical characterization reveal that the volume changes of the active material $LiNi_{0.83}Mn_{0.06}Co_{0.11}O_2$ (NMC) initiate and propagate cracks within the halide electrolyte Li_3YCl_6 (LYC), whose low fracture toughness leaves it unusually vulnerable to such damage. A fracture-mechanics framework then reveals the countervailing effects of stack pressure: although modest pressure is needed to maintain interparticle contact, further increases enhance strain transfer from the active material and thereby promote electrolyte fracture. Pressure- and particle-size-dependent experiments corroborate this framework, showing that mechanical stability can be achieved by operating within an appropriate pressure range and limiting flaw size. These principles enable stable cycling to 4.4 V at stack pressures far below those previously considered necessary and, in an anode-free pouch cell, stable operation at only 2 MPa. Our findings recast stack pressure as a mechanical boundary condition that governs competing failure modes rather than an empirical requirement to be maximized.

Operando SEM reveals mechanical failure modes

To rationally reduce stack pressure requirements while maintaining long-term cycling stability, it is essential to first understand the degradation mechanisms governing halide-based ASSBs. Detailed descriptions of the mechanical failure modes remain scarce because existing techniques, mostly postmortem analyses [12, 13] and indirect methods such as impedance spectroscopy [14], lack the spatial and temporal resolution to visualize crack initiation and evolution in real time. We bridge this gap with operando SEM, which visualizes NMC-LYC cathode composites at high resolution in real time under practically relevant ASSB operating conditions. Operando SEM was performed on the cross-section of mechanically polished NMC-LYC composite cathodes (Fig. 1a–b, Supplementary Note 1, Supplementary Fig. 2 and 3,

Supplementary Movies 1–3). The monitored composite cathode region contained no obvious pre-existing bulk defects in the pristine state (Fig. 1b). During operando measurement, the cell delivered a specific capacity of 171.3 mAh g^{-1} with an initial coulombic efficiency of 86.2% (Fig. 1c). SEM images were collected from the same region every 15 min during the first charge-discharge cycle, and representative frames were selected at the pristine state and at characteristic states during charge and discharge (Fig. 1e–f).

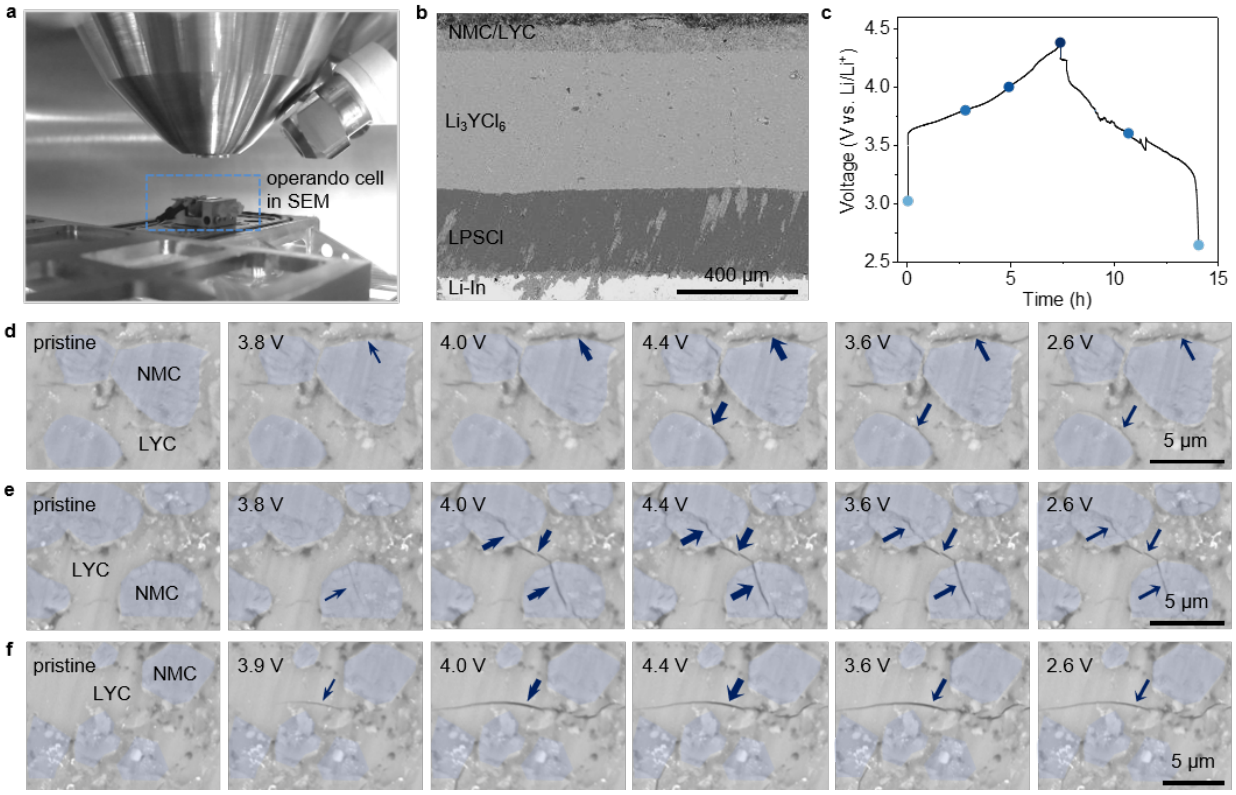


Fig. 1. Operando SEM visualization of mechanical failure modes in halide–based composite cathodes. (**a**) Photograph of the operando SEM setup with the miniature cell mounted on the SEM stage. (**b**) Cross-sectional SEM image of the full cell, consisting of an NMC–LYC composite cathode, LYC solid electrolyte layer, LPSCl interlayer, and Li–In anode. (**c**) Voltage profile of the NMC-halide cathode during operando observation. (**d**) Loss of contact between NMC and LYC;

(**e**) Crack propagation from NMC to LYC; (**f**) Crack initiation within LYC. Tests were performed at 0.2 MPa and room temperature (22–23 °C).

The time-resolved images reveal that mechanical degradation starts during charge when NMC undergoes appreciable volume change. Mechanical degradation begins at 4.0 V, coinciding with the M–H2 phase transition of NMC[15, 16]. NMC contraction induces local detachment from adjacent LYC to accommodate strain (Fig. 1d), with interfacial separation propagating along particle boundaries. By 4.4 V, ~35% of the NMC perimeter loses contact, substantially decreasing Li-ion access to the active material.

Cracking provides a second pathway for strain accommodation. Cracking within NMC and solid electrolytes has been separately reported[17-21]. Figure 1e shows that the cracks initiated within single-crystal NMC can further propagate into adjacent LYC. The induced cracks in LYC expand with charge and partially reverse upon discharge. Here, we directly capture an interfacial crack-transfer process, in which a primary NMC crack propagates into neighboring LYC and triggers secondary fracture in the electrolyte. Cracking of LYC increases the tortuosity of the ion transport pathway and hence the impedance in the composite cathode.

Cracks also develop within large LYC domains. For instance, a 12-μm-long crack is found in a 20-μm LYC domain at 4.0 V, independent of NMC cracks or contact loss (Fig. 1f). Because LYC is not expected to undergo any intrinsic volume change during cycling, these cracks likely result from tensile stress imposed by contracting NMC. When the internal cohesion energy of LYC is weaker than its interfacial adhesion to NMC, cracks occur within LYC rather than along the interface. Notably, these cracks were partially reversible, widening to 140 nm at 4.4 V and narrowing to 80 nm at 2.6 V following discharge.

In situ electrochemical impedance spectroscopy (EIS) with distribution of relaxation times (DRT) analysis reveals that these forms of mechanical degradation are the dominant degradation pathway in the NMC–LYC ASSBs (Supplementary Note 2 and Supplementary Fig. 4–5). The bulk resistance ($\tau < 10^{-4}$ s) and interphase-related impedance (γ_{CEI}, $10^{-4} < \tau < 10^{-3}$ s) remained stable throughout cycling, indicating chemical and electrochemical stability at all interfaces. In contrast, impedance associated with mechanical degradation ($\gamma_{mechanical}$, $10^{-3} < \tau < 0.1$ s) increased markedly upon cycling, likely reflecting repeated NMC volume change during (de)lithiation.

Taken together, the operando SEM observations identify three representative mechanical failure modes in NMC-LYC composite cathodes: NMC-LYC contact loss, NMC-to-LYC crack propagation, and intra-LYC cracking. These modes are not independent degradation pathways. Rather, they are competing responses to NMC-induced stress from volume change during cycling, with the local outcome determined by the relative resistance of the NMC–LYC interface to debonding and of LYC to crack propagation.

Low fracture toughness explains crack susceptibility of LYC

LYC's susceptibility to crack propagation is unusual among solid-state electrolytes. To address this issue fundamentally, we investigated its mechanical origin through nanoindentation, comparing LYC with representative sulfide and oxide electrolytes (Fig. 2).

We measured the elastic modulus (E) and hardness (H) of polished LYC pellets using a Berkovich indenter (Fig. 2a) and analyzed the data using the Oliver–Pharr method[22-24]. From the load-displacement profiles in Fig. 2b, LYC exhibits an elastic modulus of 32.1 ± 3.7 GPa, which is close to that of Li_6PS_5Cl (28.0 ± 1.8 GPa)[25] and much lower than that of $Li_7La_3Zr_2O_{12}$ (150.3 ± 2.2 GPa)[26] (Fig. 2c). Similarly, the hardness of LYC (1.30 ± 0.25 GPa) is close to that of Li_6PS_5Cl (0.92 ± 0.19 GPa)[25] and much lower than that of $Li_7La_3Zr_2O_{12}$ (9.3 ± 0.5 GPa) (Fig. 2d)[27]. The

reduced modulus and hardness likely originate from the longer ionic bonds in halides[28], which reduce lattice rigidity and enhance structural flexibility.

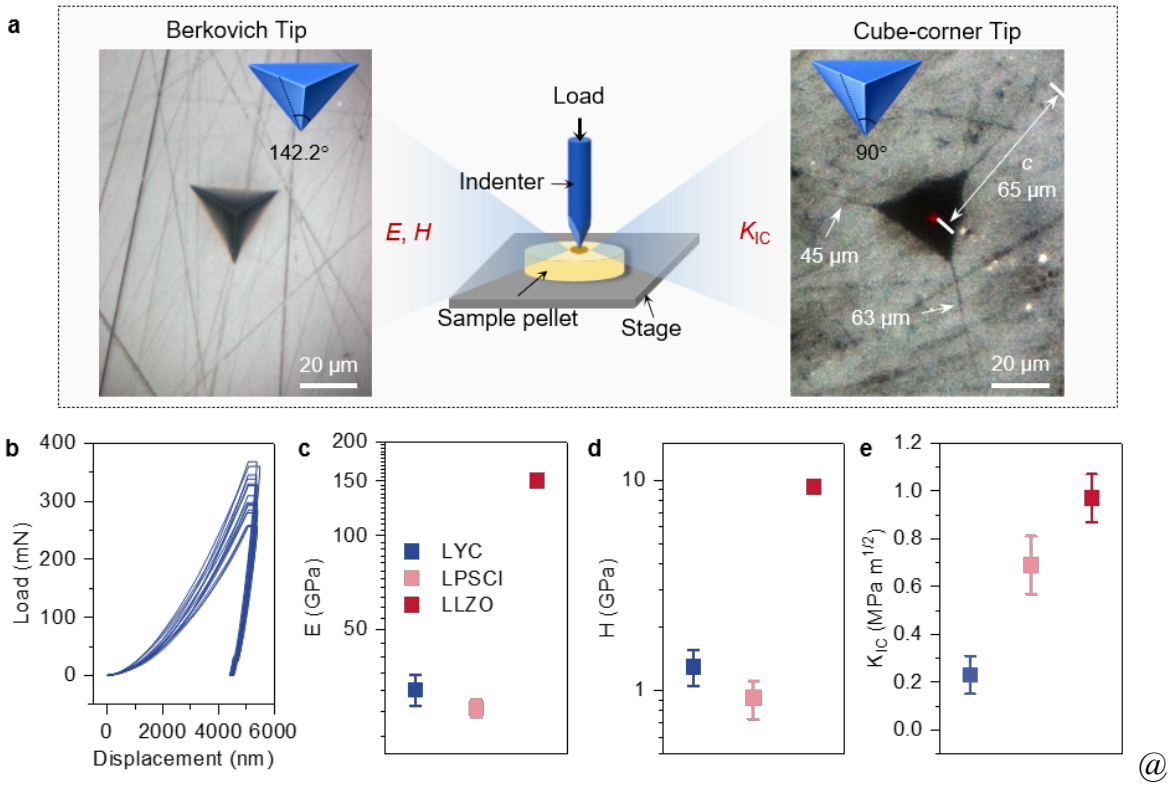


Fig. 2. Mechanical characterization of halide electrolytes. (**a**) Schematic illustration of the indentation setup. The left inset shows a Berkovich indentation mark and the geometry of a Berkovich tip with a face-to-face angle of 142.2°. The right inset shows cracks induced by a cube-corner indenter under a 400 mN load, together with the geometry of a cube-corner tip with a face-to-face angle of 90°. (**b**) Representative load-displacement curves using a Berkovich tip on LYC. (**c**–**e**) Comparison of elastic modulus (**c**), hardness (**d**), and fracture toughness (**e**) across halide, sulfide[25], and oxide[26, 27] electrolytes. Error bars represent standard deviations; n = 16 indents for elastic modulus and hardness and n = 12 indents for fracture toughness.

Fracture toughness (K_{IC}), a direct measure of crack resistance[29, 30], was determined using a cube-corner indenter that generates half-penny–shaped cracks at shallow penetration depths (Fig. 2a). Pronounced radial cracks in LYC are observed extending from the indent corners (Fig. 2a), consistent with the brittle nature of LYC. K_{IC} is calculated according to

$$K_{IC} = \alpha \left(\frac{E}{H}\right)^{\frac{1}{2}} \left(\frac{P_m}{c^{\frac{3}{2}}}\right) \quad (1)$$

where α is 0.038 for a cube-corner tip[31], E is the elastic modulus, H is hardness, P_m is the applied load, and c is the crack length from the indent center to the crack tip. The resulting K_{IC} of LYC (0.23 ± 0.08 MPa $m^{1/2}$; Fig. 2e) is substantially lower than that of sulfide Li_6PS_5Cl (LPSCl, 0.69 ± 0.12 MPa $m^{1/2}$)[25] and oxide $Li_7La_3Zr_2O_{12}$ (0.97 ± 0.1 MPa $m^{1/2}$)[27], indicating a lower resistance to crack propagation. This low fracture toughness is consistent with first-principles calculations showing that LYC possesses both a low bulk cleavage energy (W_f) and a low grain-boundary work of adhesion (W_{ad}), providing energetically accessible pathways for both transgranular cleavage and intergranular separation[32]. According to the Griffith energy criterion, a lower energy required to create new fracture surfaces facilitates crack propagation[33].

The low K_{IC} provides a mechanistic basis for the cracking-induced failure. Within the framework of linear elastic fracture mechanics, crack propagation is governed by the mode-I stress intensity factor

$$K_I = Y\sigma\sqrt{\pi a} \quad (2)$$

where Y is a dimensionless geometry factor, σ is the tensile stress acting normal to the crack plane, and a is the effective flaw size.

Under perfect interfacial bonding and complete strain transfer from NMC to LYC,

$$\sigma_{LYC} = E_{\mathrm{LYC}} \Delta\varepsilon_{\mathrm{NMC}} \quad (3)$$

where E_{LYC} is the elastic modulus of LYC and $\Delta\varepsilon_{\mathrm{NMC}}$ is the relative linear eigenstrain of NMC. In a real composite electrode, however, imperfect interparticle contact, local debonding, and stress relaxation reduce strain transfer. We therefore introduce an effective strain-transfer factor (C),

$$\sigma_{LYC} = E_{\mathrm{LYC}} C(P) \Delta\varepsilon_{\mathrm{NMC}}, 0 < C < 1 \quad (4)$$

where $C(P)$ denotes the fraction of NMC eigenstrain transmitted to LYC and may increase with stack pressure.

Stack pressure additionally reduces the crack-opening stress through crack-face compression. The effective tensile stress acting on the crack is approximated as

$$\sigma_{\mathrm{eff}} = E_{\mathrm{LYC}} C(P) \Delta\varepsilon_{\mathrm{NMC}} - \chi P \quad (5)$$

where P is the nominal stack pressure and χ is a dimensionless factor describing the fraction of P resolved as crack-closing stress. Substituting Eq. 5 into Eq. 2 gives

$$K_I = Y[E_{\mathrm{LYC}} C(P) \Delta\varepsilon_{\mathrm{NMC}} - \chi P]\sqrt{\pi a} \quad (6)$$

which applies while the effective crack-opening stress is positive and $K_I = 0$ after crack closure. Crack propagation is expected when $K_I \geq K_{IC}$.

Equation 6 highlights the dual role of stack pressure: it can increase the crack-driving stress by enhancing strain transfer through $C(P)$, while decreasing it through crack-face compression, χP. It also identifies stack pressure and flaw size as the two experimentally accessible variables governing crack propagation and thereby fracture failure in the present system. The following sections demonstrate how systematic control of these variables modulates cracking in LYC.

Stack pressure on crack propagation

To study the dual role of stack pressure on crack propagation, a quantitative understanding of $C(P)$ should be established. At very low stack pressures (e.g., ≤0.2 MPa), $C(P)$ is inferred from

operando SEM by comparing the strain in LYC in response to the volume change of NMC (Supplementary Fig. 6). The corresponding K_I of 0.15 MPa $m^{1/2}$ (Supplementary Note 3) is below LYC's K_{IC} of 0.23 MPa $m^{1/2}$, indicating an average condition where crack propagation driven by internal strain is not anticipated. At higher pressures (1−360 MPa), $C(P)$ is approximated using the pressure-dependent relative contact area A/A_0 as a first-order proxy for strain transfer because mechanical load is transmitted through interparticle contacts[34]. Under the scenarios considered (Supplementary Note 4), A/A_0 rises exponentially from ~0 to 0.2 in the low-to-medium pressure range (1–100 MPa) and approaches saturation towards unity at high pressures (>100 MPa) (Fig. 3a and Supplementary Fig. 7a). Substituting the resulting contact-area-based approximation of $C(P)$ into Eq. 6 gives a non-monotonic $K_I(P)$: K_I initially increases with pressure, reaches a maximum at intermediate-to-high pressures, and subsequently declines at high pressures, reflecting the competition between a saturating $C(P)$ and a continuously increasing χP. The pressure range over which K_I stays below K_{IC} depends heavily on the fracture toughness of the electrolytes (e.g., 0.23 MPa $m^{1/2}$ for LYC vs 0.69 MPa $m^{1/2}$ for LPSCl); under some scenarios, K_I never reaches the K_{IC} of LPSCl (Supplementary Fig. 7b). Although the exact K_I values depend on the approximated $C(P)$, the analysis consistently predicts a substantially reduced propensity for fracture at low stack pressures and a narrow fracture-avoiding pressure range for electrolytes with low fracture toughness.

The effect of stack pressure on the mechanical integrity of the electrolyte and its impact on cycling performance is investigated with NMC–Li die cells (Supplementary Fig. 8) cycled under 2, 8, 14 and 21 MPa. Pressures higher than 21 MPa were not examined because they increase the risk of Li penetration through the electrolyte[35, 36]. As shown in Fig. 3b, NMC specific capacities exceed 200 mAh g^{-1} when cycled at 8 and 14 MPa stack pressure, but only exhibit ~190 mAh g^{-1} at 2 and 21 MPa. Cycling data (Fig. 3b) show that moderate pressures (14 MPa) improve capacity

retention relative to both lower and higher pressures. Cells at 14 MPa retain 82% of initial capacity after 1,000 cycles at 1C and 30 °C (Fig. 3c, Supplementary Fig. 9), demonstrating stable operation at 4.4 V, consistent with the predicted balance between interfacial debonding and electrolyte fracture.

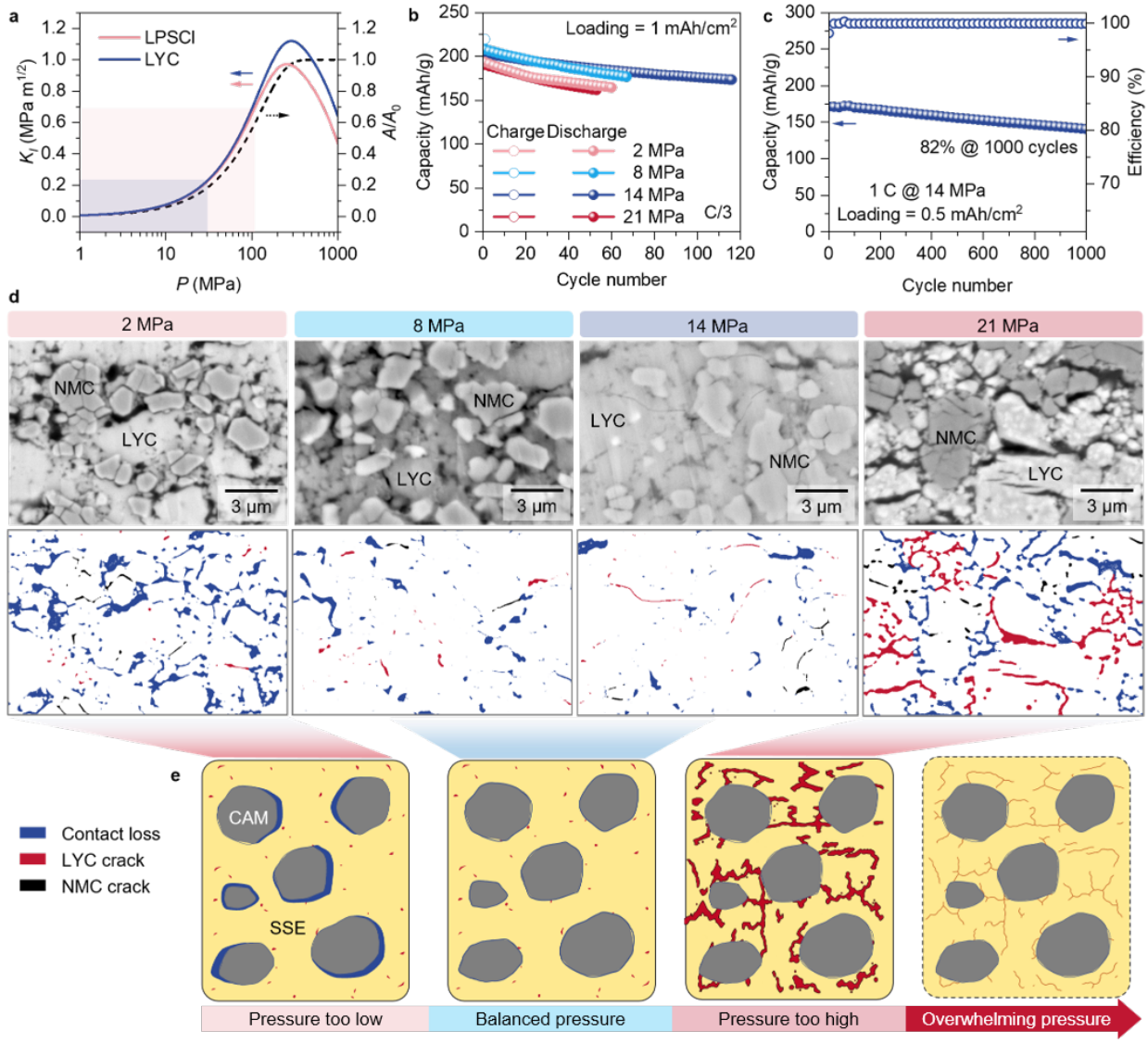


Fig. 3. Impact of stack pressure on mechanical degradation modes in halide composite cathodes. (**a**) Pressure-dependent K_I for halide and sulfide solid electrolytes; shaded areas indicate the stack pressure range where K_I is lower than the corresponding K_{IC} (0.23 and 0.69 MPa m$^{1/2}$ for LYC and LPSCl, respectively). (**b**) Cycling stability at stack pressures of 2, 8, 14, and 21 MPa

until 80% capacity retention. Cell structure is $Li_{0.93}Mg_{0.03}$|LPSCl|LYC|NMC–LYC. (**c**) Long-term cycling at 14 MPa and 30 °C, retaining 82% of initial capacity after 1,000 cycles at 0.5 mA cm^{-2}. (**d**) Cross-sectional SEM and corresponding segmented images after cycling under different stack pressures. (**e**) Schematic summary of the stack-pressure-dependent mechanical degradation modes in NMC–LYC composite cathodes.

Post-mortem cross-sectional SEM clarifies the origin of this pressure dependence (Fig. 3d and Supplementary Fig. 10–11). The pristine cathode shows conformal NMC–LYC contact. After cycling at 2 MPa, extensive NMC–LYC contact loss develops (blue regions), consistent with insufficient mechanical constraint and the observation by operando SEM. At 8–14 MPa, contact loss is reduced, but microcracks appear within the electrolyte (red regions). At 21 MPa, cracks widen to sub-micrometer scales and disrupt the percolated ion-transport network. Continued cycling under high pressure caused electrolyte pulverization, characterized by dense microcrack networks (Supplementary Fig. 11a) and a void fraction increase from 0.7% (Supplementary Fig. 10b) to 31% (Supplementary Fig. 11b).

These results corroborate the mechanistic analysis that high stack pressures increase strain transfer and therefore promote crack propagation. They also reveal that low pressures, although reducing fracture, induce a competing failure mechanism due to a pressure-dependent competition between NMC–LYC interfacial debonding and LYC crack propagation.

The stack-pressure dependence of mechanical failure of LYC composite electrodes can now be established (Fig. 3e). At extremely low stack pressures, interfacial debonding is the dominant mechanical failure path. Moderate pressures alleviate interfacial debonding but remain insufficient to drive unstable crack propagation. Beyond a certain pressure threshold, stack

pressure drives K_I beyond K_{IC} and makes fracture the dominant failure mechanism. Very high stack pressures compress fractured electrolyte particles and close the gaps formed from fracturing, thereby partially restoring physical contact without reversing the underlying fracture. The exact pressure values of these ranges vary by system. This framework provides a mechanistic explanation for the overwhelming choice of high stack pressures for halide-based ASSBs as the means to reverse the contact loss induced by fracture. Our results show that minimizing fracture, rather than compensating for its consequences with high stack pressure, enables stable cycling at substantially lower pressures.

Flaw size on crack propagation

Having established the role of stack pressure, we next examine flaw size—the other experimentally adjustable parameter controlling crack propagation in Eq. 6. Because K_I scales with the square root of flaw size, LYC with smaller flaw sizes is more likely to avoid crack propagation and eventual failure. Flaws in LYC range from surface defects on LYC particles to interparticle voids, and LYC particle size limits the maximum flaw size that can exist within an individual particle. Small LYC particles should therefore be more resistant to cracking. To test this particle size dependence of cracking, we statistically analyzed fractured LYC particles from operando SEM images (Supplementary Fig. 12). Internal fractures occur preferentially in larger LYC particles or continuous LYC-rich domains, whereas smaller LYC particles exhibit a substantially lower tendency to fracture. This trend supports a flaw size-controlled fracture picture: larger domains statistically have a higher probability of containing larger critical flaws and are more prone to fracture during NMC-driven deformation.

Motivated by this observation, we reduced the LYC catholyte particle size by high-energy ball milling. The pristine LYC powder contained large particles of approximately 8 μm together

with surface-attached submicron particles, whereas ball milling reduced the large-particle size to approximately 3 μm (Supplementary Fig. 13). To assess the particle-size effect, cells using pristine and downsized LYC powders were cycled under the same stack pressure of 14 MPa. The two cells showed similar first-cycle voltage profiles (Supplementary Fig. 14a), indicating comparable initial electrochemical utilization. However, the downsized LYC catholyte delivered more stable cycling (Supplementary Fig. 14b), and DRT analysis showed a lower interfacial-resistance contribution (Supplementary Fig. 15). These results indicate that particle downsizing mitigates mechanically induced impedance growth, most likely by reducing the probability of large-flaw-controlled fracture, while the improved particle-size uniformity may further promote a more homogeneous composite microstructure.

The pressure-dependence discussed above alters the crack-driving force, whereas particle size alters the flaw size entering Eq. 6. Together, these two variables define the experimentally accessible design space for suppressing fracture.

Anode-free pouch cell demonstration at a low stack pressure

The stack-pressure and particle-size design principles identified above are next implemented in an anode-free pouch-cell architecture to demonstrate robust performance under low stack pressure. Unlike the die-cell configuration, the pouch cell design (Fig. 4a) employs warm isostatic pressing (WIP), which improves electrode densification and mechanical integrity[37, 38], together with a compliant silicone-rubber pressure jig that provides more uniform pressure during cycling (Supplementary Fig. 16)[39]. With these design improvements, stable operation was achieved at a stack pressure of only 2 MPa.

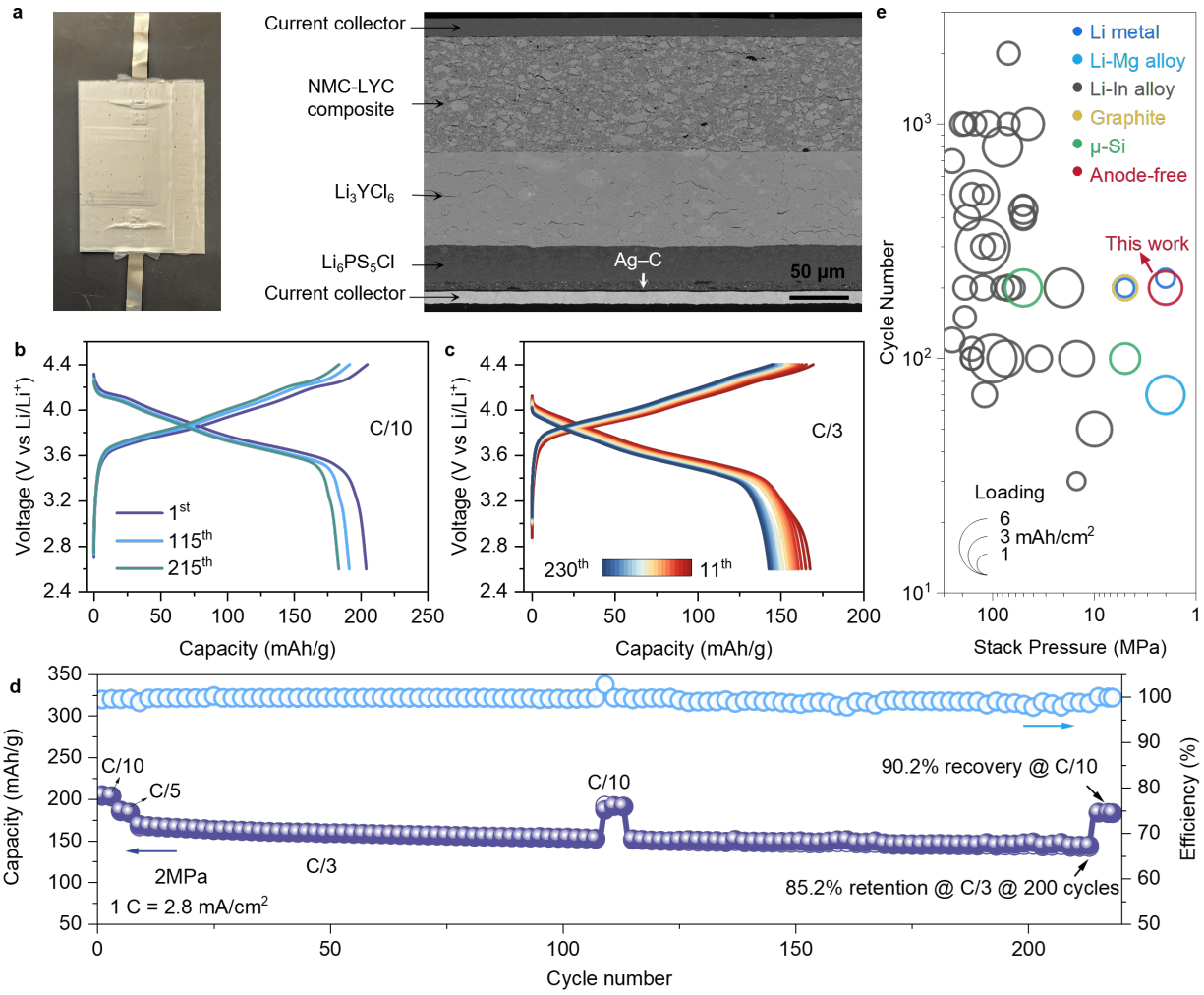


Fig. 4. Electrochemical performance of anode-free pouch cells. (**a**) Photograph and corresponding cross-sectional SEM image of the anode-free pouch cell, showing the multilayer architecture of the NMC–LYC composite cathode, LYC electrolyte layer, LPSCl separator and Ag–C interlayer. (**b**, **c**) Representative voltage profiles collected at C/10 (**b**) and C/3 (**c**) within a voltage window of 2.6–4.4 V. (**d**) Cycling performance of the anode-free pouch cell. The cell was tested under an external stack pressure of 2 MPa at 45 °C. (**e**) Visual comparison of stack pressure, cycle life, and areal loading of reported halide-based solid-state batteries. Circle size indicates areal loading, and circle color denotes the anode type.

The anode-free pouch cell delivered an initial C/10 discharge capacity of 204.1 mAh g^{-1} (Fig. 4b), comparable to those of die cells. The minimal overpotential growth in the C/10 cycles and nearly overlapping voltage profiles during C/3 cycling are consistent with minimal mechanically induced impedance growth (Fig. 4b,c). Notably, the pouch cell retains 85.2% of its

capacity after 200 cycles at C/3 and exhibits a 90.2% capacity recovery when cycled back to C/10 (Fig. 4d).

These pouch-cell results demonstrate that halide ASSBs can operate at substantially lower external pressures than previously appreciated. A comparison with reported halide ASSBs further contextualizes this finding (Fig. 4e and Supplementary Table 1). Many long-cycling halide cells relied on high stack pressures to maintain particle contact, whereas lower-pressure studies often reduced the upper cutoff voltage to reduce active material eigenstrain[40]. In contrast, the present pouch-cell design combines a high cutoff voltage, an anode-free configuration and low stack pressure. This distinction is central for practical cell design: the combination of high-voltage cathode and lightweight anode for high energy density, with only modest stack pressure to maintain cycling stability.

Discussion

The present findings suggest that stack pressure in halide solid-state batteries should be viewed as a mechanical boundary condition governing fracture rather than an empirical target to be maximized. Within the fracture-mechanics framework developed here, nominal pressure does not uniquely determine mechanical stability: it affects both strain transfer from the active material and crack-face compression, while the resulting stress intensity further depends on flaw size and geometry. A single stack-pressure requirement therefore cannot be considered an intrinsic property of a halide electrolyte; instead, it reflects the mechanical environment created by a particular electrode and cell configuration. Accordingly, the favorable performance at 14 MPa in die cells represents a balance between contact retention and fracture under those specific conditions, rather than a universal optimum for LYC. Likewise, the pouch-cell result does not establish 2 MPa as an optimum, but demonstrates that stable operation is possible far below the pressures conventionally

employed when fabrication and pressure application are altered. How nominal stack pressure translates into local stress and strain transfer across different cell architectures therefore warrants greater attention than the nominal pressure alone.

This work also provides a basis for interpreting existing approaches to low-pressure halide ASSBs. Researchers have pursued mechanically compliant oxyhalide electrolytes and the incorporation of compliant phases into composite cathodes to accommodate active-material deformation and reduce pressure requirements. Fracture mechanics offers a more general interpretation of such strategies: mechanical stability can be improved by reducing the crack-driving force, limiting the size of critical flaws, or increasing resistance to crack propagation. Importantly, these variables need not be controlled through electrolyte composition alone. Particle dimensions, interfacial mechanics, and composite microstructure provide alternative means of suppressing fracture without necessarily modifying the electrolyte chemistry and compromising its electrochemical stability, ionic conductivity, or materials simplicity. This broader design space shifts the emphasis from developing an electrolyte that is intrinsically more compliant to engineering how deformation and fracture occur within the composite electrode. More generally, in heterogeneous solid-state electrochemical systems that couple volume-changing active materials with brittle ion-conducting phases, external compression should not be assumed to be uniformly stabilizing. Although compression can preserve interfacial contact and close existing cracks, it can also increase the transfer of internally generated strain and thereby promote fracture. The balance between these effects will depend on the fracture resistance, flaw population, interfacial mechanics and microstructure of the constituent materials. In halide solid-state batteries, accounting for this balance provides a route towards stable low-pressure operation based on intrinsic electrode stability rather than sustained external constraint.

The present analytical treatment is necessarily a first-order description of this heterogeneous mechanical environment. In particular, the effective strain-transfer factor, $C(P)$, remains difficult to determine quantitatively over practical pressure ranges, while local flaw geometry, crack orientation and stress heterogeneity are simplified in the current model. Direct measurements of pressure-dependent strain transfer and local stress, coupled with statistical characterization of flaw populations and operando three-dimensional fracture evolution, will be important for developing predictive fracture criteria for composite electrodes. Nevertheless, identifying these governing variables already shifts the design objective from using external compression to compensate for mechanical damage toward suppressing the formation and propagation of critical fractures. Reducing this reliance on stack pressure could relax cell-packaging requirements and facilitate high-energy architectures based on lithium metal or anode-free designs, mitigating the system-level penalties that currently accompany high-pressure operation. Mechanically informed control of fracture may therefore provide a route toward halide solid-state batteries whose practical operation is enabled by intrinsic electrode stability rather than sustained external constraint.

Methods

Materials and synthesis

LYC was synthesized by first hand-mixing 1.5 g of LiCl (BTC, anhydrous, 99.995%) and 2.54 g of YCl_3 (Thermo Scientific Chemicals, 99.99%) in an agate mortar for 10 minutes. The mixture was then transferred to an 80 mL ZrO_2 ball-milling jar with a 40:1 mass ratio of ZrO_2 milling media (Φ 3 mm) to precursor powder. We performed mechanochemical synthesis in a planetary micro-mill (Pulverisette 7, Fritsch) at 500 rpm for 195 cycles of 15 min milling followed by 5 min

rest. After every 65 cycles, the jar was opened in a glovebox, and the caked precursor layers were scraped off and re-homogenized to ensure uniform mixing.

Single-crystal $LiNi_{0.83}Mn_{0.06}Co_{0.11}O_2$ (MSE Supplies) served as the cathode active material, and vapor-grown carbon fibers (VGCF, PR-19-XT-HHT, Applied Sciences) were used as a conductive additive in the composite cathode. Li_6PS_5Cl (MSE Supplies) functioned as a separating layer. $Li_{0.97}Mg_{0.03}$ (Li-Mg, 100 μm, MSE Supplies) was used as the anode, offering good contact with Li_6PS_5Cl layer. For operando cells, a Li-In anode was prepared by mechanically rolling indium ingot (Sigma Aldrich) and Li foil (Alfa Aesar) at a 2:1 molar ratio.

Cell fabrication and electrochemical characterization

Die cell: First, 50 mg of Li_6PS_5Cl was placed into a polyether-ether-ketone (PEEK) mold with a diameter of 12.7 mm and densified at 150 MPa for 2 min. Then, 100 mg of LYC was spread over one side of the pellet and pressed at 150 MPa for 2 min. The composite cathode was prepared by mixing NMC, LYC, and VGCF in a 50:47:3 mass ratio. The composite cathode powders were evenly spread on the LYC side of the pellet for an active mass loading of 5 or 2.5 mg/cm^2, corresponding to 1 or 0.5 mAh/cm^2, and densified at 375 MPa for 10 min. A $Li_{0.93}Mg_{0.03}$ foil (9 mV vs Li/Li$^+$) was used as the Li anode and pressed on the Li_6PS_5Cl side of the electrolyte pellet at 75 MPa for 1 min to ensure intimate contact. The formed cells were assembled in spring-loaded holders to maintain constant pressure; the pressure fluctuation over the cycling period is within ±3%. Galvanostatic cycling was performed at 30 °C in a climate-controlled oven in the 2.6−4.4 V (vs. Li/Li$^+$) voltage range, starting with two formation cycles at C/10 followed by cycling at C/3 or 1C (1C = 200 mA g^{-1}). EIS spectra were collected from 1 MHz to 100 mHz with a 7-mV amplitude. *In situ* EIS measurements were collected at 15 min intervals during the cycling. Supplementary Fig. 17 shows negligible voltage drop during measurement, confirming that the measured cell voltage corresponds to the true cathode potential. The DRT profile (γ(t)) was derived

from the measured impedance spectra by numerically solving the discretized form of the DRT integral equation using open-source DRT software[41], using regularization parameter of 10^{-3} and an FWHM coefficient of 0.5.

Pouch cell: The dry process was employed to fabricate the NMC-LYC composite cathode as well as the electrolyte film. The composite cathode was prepared by mixing NMC, LYC, VGCF and PTFE in a 50:47:2.5:0.5 mass ratio, followed by hand-roll pressing into a thickness of ~100 μm and a mass loading of ~14 mg/cm^2. To fabricate the electrolyte films, 99.5% SSE powder and 0.5% PTFE were first mixed, and then hand-roll-pressed into a freestanding film. LPSCl membrane[42] and Ag-C interlayer[43] were prepared following procedures in our previous report. Then, the NMC-LYC cathode layer, LYC and LPSCl membranes, and an Ag-C layer coated on Cu foil were pressed together to form an all-solid-state pouch cell (Fig. 4a). Cross-sectional SEM shows the multilayer architecture consisting of a 100-μm-thick NMC-LYC composite cathode, an 80-μm-thick LYC and a 30-μm-thick LPSCl SSE layers (Fig. 4a). The electrochemical performance of pouch cells was evaluated at 45 °C under an external pressure of approximately 2 MPa.

Ionic conductivity measurement of composite cathode

The ionic conductivity of the composite cathode was measured using an electron-blocking five-layer cell via DC polarization[44]. Approximately 100 mg composite cathode powder was first densified at 375 MPa for thickness measurement. Two layers of Li_6PS_5Cl (50 mg) were added to both sides and densified again at 375 MPa. Li metals were attached to both sides of the Li_6PS_5Cl layers, forming a five-layer Li|Li_6PS_5Cl|Cathode|Li_6PS_5Cl|Li structure. The cell current was measured under applied voltages of 5, 10, 20, and 30 mV (Supplementary Fig. 17a). The ionic resistance, R_{ion}, was determined from the slope of the voltage–current relationship by linear fitting according to Ohm's law (Supplementary Fig. 17b). The ionic conductivity of the composite

cathode, σion was then calculated as $\sigma_{ion} = L/(R_{ion}A)$, where L is the thickness of the composite cathode pellet and A is the area.

Operando cross-sectional SEM characterization

Operando cells were fabricated following the procedure for die cells except that a Li-In foil was used as the anode which was pressed onto the Li_6PS_5Cl layer at 150 MPa. As-prepared Li-In|LPSC|LYC|NMC:LYC cells were removed from the PEEK die and tailored to a 3 mm × 3 mm miniature cell. Ex-situ cross-sections were prepared by an Ar^+-ion cross-section polisher (IB-19520CCP, JEOL, USA) at ~50 μm h^{-1} and –30 °C to minimize heat damage. For operando experiments, cross-sections were mechanically polished with 10,000-grit sandpaper to avoid Ar^+-induced LYC reduction. The miniature cells were mounted in an air-free vessel (Solid Design Instruments, Model FV-003A, Supplementary Fig. 18) under 0.2 MPa stack pressure applied by a plastic bolt and calibrated torque wrench (Imada, DID-05). The vessel was loaded into an SEM (Axia ChemiSEM) and connected to a potentiostat (Biologic SP300). Cycling was performed at room temperature (22–23 °C) with the current density of 0.1 mA/cm^2. SEM images were captured every 15 min at the same location. ImageJ with Trainable Weka Segmentation Tool was used to analyze particle-level volume changes and create operando videos.

Modulus and hardness measurement from Berkovich indenter

An Agilent G200 nano-indenter, installed inside an argon-filled glovebox, with a diamond Berkovich tip having the effective cone angle of 70.3° was used to measure the elastic modulus and hardness of LYC pellets densified at 375 MPa. A depth-controlled continuous stiffness method (CSM) at a constant strain rate was employed for this study. This method measures the contact stiffness (S) as a function of indentation depth (h_c) by applying the oscillatory force to the tip, $P = P_0 e^{i\omega t}$ and measuring the displacement amplitude and phase $h_c = h_0 e^{i\omega t+\varphi}$ using lock-in

amplifier. The pellet surfaces were mechanically polished with 2400 grit sandpaper to produce smooth and pore-free surfaces. A maximum indentation depth of 5 μm was selected to minimize the influence of surface roughness on the resulting modulus and hardness. The indentation strain-rate of 0.05 s^{-1} and a displacement amplitude of 1 nm was used for the measurements. A 4×4 array of indents, each spaced 200 μm apart, was made near the center of the pellets. The elastic modulus and hardness are then calculated based on Oliver–Pharr method using Eqs. 8–10, and the results were averaged over 16 indents.

The reduced elastic modulus can be calculated by

$$E_r = \frac{\sqrt{\pi}\, S}{2\,\beta\,\sqrt{A}} \tag{7}$$

where $\beta = 1.034$ for triangular cross-sections such as the Berkovich indenter and A is the projected contact area determined through a calibration procedure performed on center fused silica using the Oliver–Pharr method. The reduced elastic modulus is converted into Young's modulus by

$$\frac{1}{E_r} = \frac{1-\nu^2}{E} + \frac{1-\nu_i{}^2}{E_i} \tag{8}$$

where E and ν are the Young's modulus and Poisson's ratio of the test sample, respectively, and E_i and ν_i are the Young's modulus and Poisson's ratio of the indenter. Data are reported as mean ± standard deviation.

The hardness H is calculated by

$$H = \frac{P_{max}}{A} \tag{9}$$

where P_{max} is the maximum load and A is the projected contact area at P_{max}.

Fracture toughness measurements using a cube corner diamond indenter

Indentation techniques were also applicable to measure the fracture toughness of a material by measuring the radial crack length generated during indentation. The fracture toughness of the LYC pellet was measured from a sharp cube corner diamond indenter having an effective cone angle of

42.28°. The cube corner indenter can penetrate greater depth into the material for a given load as compared to the Berkovich indenter. Therefore, higher stresses are induced beneath the indenter that help generate relatively large cracks even at low load. A maximum load of 400 mN was applied to the LYC pellet at twelve different locations to initiate radial cracking. All crack indents in this study were captured using a microscope on the G200 nanoindenter and crack length was measured using ImageJ software. The fracture toughness (K_{IC}) was calculated using the relation of Lawn *et al.* for half-penny cracks under the indent[45].

Data availability:

All data in this work are available in the text and Supplementary Information. Source data are provided with this paper.

References:

1. Janek J, Zeier WG. Challenges in speeding up solid-state battery development. *Nat Energy* **8**, 230-240 (2023).

2. Zhao LH, Lakraychi AE, Chen ZY, Liang YL, Yao Y. Roadmap of Solid-State Lithium-Organic Batteries toward 500 Wh kg^{-1}. *ACS Energy Lett* **6**, 3287-3306 (2021).

3. Nikodimos Y, Su WN, Hwang BJ. Halide Solid-State Electrolytes: Stability and Application for High Voltage All-Solid-State Li Batteries. *Adv Energy Mater* **13**, 1-36 (2023).

4. Wang S*, et al.* Lithium Chlorides and Bromides as Promising Solid-State Chemistries for Fast Ion Conductors with Good Electrochemical Stability. *Angew Chem Int Ed* **58**, 8039-8043 (2019).

5. Lee YG*, et al.* High-Energy Long-Cycling All-Solid-State Lithium Metal Batteries Enabled by Silver-Carbon Composite Anodes. *Nat Energy* **5**, 299–308 (2020).

6. Chen ZY*, et al.* Manipulating Hardness to Construct Favorable Electrode Microstructures for All-Solid-State Batteries. *Adv Energy Mater* **14**, 2403050 (2024).

7. Zhao LH*, et al.* Imaging the Evolution of Lithium-Solid Electrolyte Interface Using Operando Scanning Electron Microscopy. *Nat Commun* **16**, 4283 (2025).

8. Yun J*, et al.* Deciphering the critical degradation factors of solid composite electrodes with halide electrolytes: Interfacial reaction versus ionic transport. *Energy Storage Mater* **59**, 102787 (2023).

9. Palmer M*, et al.* Conformal hetero-electrolyte interface between soft oxyhalides and garnet enables low-pressure lithium-reservoir-free solid-state batteries. *Energy Environ Sci* **19**, 3283-3299 (2026).

10. Dai T*, et al.* Inorganic glass electrolytes with polymer-like viscoelasticity. *Nat Energy* **8**, 1221-1228 (2023).

11. Huang Q*, et al.* A New Route to High-Performance Halide-Based Solid-State Batteries: Perfluoropolyether Enables Ion Transport Expansion and Interfacial Protection. *Adv Energy Mater* **16**, e70963 (2026).

12. Han Y*, et al.* Single- or Poly-Crystalline Ni-Rich Layered Cathode, Sulfide or Halide Solid Electrolyte: Which Will be the Winners for All-Solid-State Batteries? *Adv Energy Mater* **11**, 2100126 (2021).

13. Yan PF, Zheng JM, Gu M, Xiao J, Zhang JG, Wang CM. Intragranular Cracking as a Critical Barrier for High-Voltage Usage of Layer-Structured Cathode for Lithium-Ion Batteries. *Nat Commun* **8**, 14101 (2017).

14. Cheng EJ, Kanamura K, Kushida Y, Abe T. Degradation Mechanism of All-Solid-State Li-Metal Batteries Studied by Electrochemical Impedance Spectroscopy. *ACS Appl Mater Interfaces* **14**, 40881-40889 (2022).

15. Zhang SS. Problems and Their Origins of Ni-Rich Layered Oxide Cathode Materials. *Energy Storage Mater* **24**, 247-254 (2020).

16. Nuroldayeva G, Adair D, Bakenov Z, Uzakbaiuly B. Revealing Phase Transition in Ni-Rich Cathodes via a Nondestructive Entropymetry Method. *ACS Omega* **8**, 37899-37907 (2023).

17. Shishvan SS, Fleck NA, Mcmeeking RM, Deshpande VS. Cracking and Associated Volumetric Expansion of NMC811 Secondary Particles. *J Power Sources* **588**, 233745 (2023).

18. Heenan TMM*, et al.* Identifying the Origins of Microstructural Defects Such as Cracking within Ni-Rich NMC811 Cathode Particles for Lithium-Ion Batteries. *Adv Energy Mater* **10**, 2002655 (2020).

19. Hu JT*, et al.* Mesoscale-Architecture-Based Crack Evolution Dictating Cycling Stability of Advanced Lithium Ion Batteries. *Nano Energy* **79**, 105420 (2021).

20. Gao H*, et al.* Visualizing the failure of solid electrolyte under GPa-level interface stress induced by lithium eruption. *Nat Commun* **13**, 5050 (2022).

21. Ning Z*, et al.* Visualizing plating-induced cracking in lithium-anode solid-electrolyte cells. *Nat Mater* **20**, 1121-1129 (2021).

22. Tsui TY, Oliver WC, Pharr GM. Indenter Geometry Effects on The Measurement of Mechanical Properties by Nanoindentation with Sharp Indenters. *MRS Proc* **436**, 147-152 (1996).

23. Yoshida S, Sawasato H, Sugawara T, Miura Y, Matsuoka J. Effects of Indenter Geometry on Indentation-Induced Densification of Soda-Lime Glass. *J Mater Res* **25**, 2203-2211 (2010).

24. Oliver WC, Pharr GM. An Improved Technique for Determining Hardness and Elastic-Modulus Using Load and Displacement Sensing Indentation Experiments. *J Mater Res* **7**, 1564-1583 (1992).

25. Ning ZY*, et al.* Dendrite Initiation and Propagation in Lithium Metal Solid-State Batteries. *Nature* **618**, 287-293 (2023).

26. Yu S*, et al.* Elastic Properties of the Solid Electrolyte $Li_7La_3Zr_2O_{12}$ (LLZO). *Chem Mater* **28**, 197-206 (2016).

27. Kim Y, Jo H, Allen JL, Choe H, Wolfenstine J, Sakamotok J. The Effect of Relative Density on the Mechanical Properties of Hot-Pressed Cubic $Li_7La_3Zr_2O_{12}$. *J Am Ceram Soc* **99**, 1367-1374 (2016).

28. Wang CH, Liang JW, Kim JT, Sun XL. Prospects of Halide-Based All-Solid-State Batteries: From Material Design to Practical Application. *Sci Adv* **8**, eadc9516 (2022).

29. Hempel JL, Meyer A, Hill R, Cheng YT. Validating a Facile Approach to Measuring Fracture Toughness by Instrumented Indentation Without Imaging Crack-Lengths. *MRS Commun* **12**, 279-282 (2022).

30. Yuan CH, Lu WQ, Xu J. Unlocking the Electrochemical-Mechanical Coupling Behaviors of Dendrite Growth and Crack Propagation in All-Solid-State Batteries. *Adv Energy Mater* **11**, 211807 (2021).

31. Bruns S, Petho L, Minnert C, Michler J, Durst K. Fracture Toughness Determination of Fused Silica by Cube Corner Indentation Cracking and Pillar Splitting. *Mater Des* **186**, 108311 (2020).

32. Xie WH, Deng ZY, Liu ZY, Famprikis T, Butler KT, Canepa P. Effects of Grain Boundaries and Surfaces on Electronic and Mechanical Properties of Solid Electrolytes. *Adv Energy Mater* **14**, 2304230 (2024).

33. Griffith AA. The Phenomena of Rupture and Flow in Solids. *Philos Trans R Soc Lond A* **221**, 163-198 (1921).

34. Tian H-K, Qi Y. Simulation of the Effect of Contact Area Loss in All-Solid-State Li-Ion Batteries. *J Electrochem Soc* **164**, E3512 (2017).

35. Zhao LH*, et al.* Taming Metal-Solid Electrolyte Interface Instability via Metal Strain Hardening. *Adv Energy Mater* **13**, 2300679 (2023).

36. Doux JM*, et al.* Stack Pressure Considerations for Room-Temperature All-Solid-State Lithium Metal Batteries. *Adv Energy Mater* **10**, 1903253 (2020).

37. Dixit M*, et al.* The Role of Isostatic Pressing in Large-Scale Production of Solid-State Batteries. *ACS Energy Lett* **7**, 3936-3946 (2022).

38. Dixit M*, et al.* Isostatic Pressing of Multilayer Pouch Cells and Its Implications for Battery Manufacturing. *Device* **2**, 100370 (2024).

39. Thorpe MA*, et al.* Controlling Stack Pressure Inhomogeneity in Anode-Free Solid-State Batteries Using Elastomeric Interlayers. *Matter* **8**, 101955 (2025).

40. Gao XW*, et al.* Solid-state lithium battery cathodes operating at low pressures. *Joule* **6**, 636-646 (2022).

41. Wan TH, Saccoccio M, Chen C, Ciucci F. Influence of the Discretization Methods on the Distribution of Relaxation Times Deconvolution: Implementing Radial Basis Functions with DRTtools. *Electrochim Acta* **184**, 483-499 (2015).

42. Emley B*, et al.* Isostatic Pressing of Multilayer Pouch Cells and Its Implications for Battery Manufacturing. *Mater Today Phys* **18**, 100397 (2021).

43. Wu C*, et al.* Understanding the Chemomechanical Function of the Silver–Carbon Interlayer in Sheet-type All-Solid-State Lithium–Metal Batteries. *Nano Lett* **23**, 4415-4422 (2023).

44. Emley B*, et al.* Impact of Fabrication Methods on Binder Distribution and Charge Transport in Composite Cathodes of All-Solid-State Batteries. *Mater Futures* **2**, 045102 (2023).

45. Lawn BR, Evans AG, Marshall DB. Elastic-Plastic Indentation Damage in Ceramics: The Median-Radial Crack System. *J Am Ceram Soc* **63**, 574-581 (1980).

Acknowledgments:

This work was supported by the US Department of Energy's Office of Energy Efficiency and Renewable Energy under the Vehicle Technologies Program under Prime Contract No. DE-ACO5-000R2275.

Author contributions:

L.G., J.Z., and L.Z. conceived the original idea. Y.Y., J.N., and R.S. directed the work. L.G., J.Z., and L.Z. designed the experiments. J.Z., L.G., and L.Z. analyzed and discussed the experimental data. S.T. helped with the mechanical measurements. J. Z. performed the pouch cell assembly and tests. P.T. and M.L. conducted the DRT code. Y.L., L.G., J.Z., and L.Z. wrote the initial draft, and all authors contributed to the writing of the final manuscript.

Competing interests:

Y.Y. has equity interests in LiBeyond, LLC and Solid Design Instruments, LLC. Y.L. has equity interests in LiBeyond, LLC. The remaining authors declare no competing interests.